Electronic Supporting Information

Experimental and theoretical investigation of a mesoporous K_xWO_3 material having superior mechanical strength

Sonal Dey,*‡[a] Sean T. Anderson,[a] Robert A. Mayanovic,[a] Ridwan Sakidja,[a] Kai Landskron,[b] Berenika Kokoszka,[b] Manik Mandal,[b] and Zhongwu Wang[c]

[a]*Department of Physics, Astronomy & Materials Science, Missouri State University, Springfield, MO 65897, USA.*
[b]*Department of Chemistry, Lehigh University, Bethlehem, PA 18015, USA.*
[c]*Cornell High Energy Synchrotron Source, Wilson Laboratory, Cornell University, Ithaca, NY 14853, USA.*
* sdey@sunypoly.edu
‡ *Current address: Colleges of Nanoscale Science and Engineering, State University of New York Polytechnic Institute, Albany, NY 12203, USA*

Scanning Electron Microscopy

An FEI Quanta 200 FEG Scanning Electron Microscope (SEM) was used for SEM imaging of samples of the mesoporous $K_{0.07}WO_3$ material. The energy dispersive x-ray spectroscopy measurements (SEM-EDX) were made using focused electron beam of energy 20 keV and an energy dispersive detector connected to the SEM. The SEM-EDX data and an SEM image of the mesoporous $K_{0.07}WO_3$ material are shown in Fig. 1b.

Transmission Electron Microscopy

TEM images were collected from the as-synthesized periodic FDU-12-type mesoporous $K_{0.07}WO_3$ sample at the University of Arkansas Nano-Bio Materials Characterization Facility using a Titan 80-300 with the field emission gun operated at 300 keV. The simulated selected area electron diffraction (SAED) patterns were generated from the TEM images using the fast Fourier filtering (FFT) within the imageJ software. The meso-scale ordering is clearly observed in a TEM image (Fig. 1a) of an individual sub-micron sized particle of the mesoporous $K_{0.07}WO_3$ material. Select-area energy-dispersive x-ray spectroscopy (EDX) showed the presence of K in individual sub-micron sized particles of

mesoporous $K_{0.07}WO_3$. The detection of P using EDX was prohibitive due to the strong overlap between the P K_α and W M_α emission lines.

The TEM measurements were performed on the remnants of the mesoporous K_xWO_3 sample after subjecting to pressure in the diamond anvil cell to ~ 18.5 GPa using a JEOL JEM-ARM200CF instrument operated at an accelerating voltage of 60 kV. A representative TEM image of the sample after exposing to high pressures is shown in Fig. 1c. The Fast Fourier Transform (FFT) of the TEM image (Fig. 1c inset) shows that the crystalline layered structure of the framework is preserved after subjecting the material to high pressures. The structure evident in the TEM image is consistent with the original monoclinic WO_3 phase.

SAXS Data Analysis

The face-centered cubic mesopores structure, having $Fm\bar{3}m$ symmetry group designation, was confirmed from the ratios of first: second: third peaks in the small angle x-ray scattering (SAXS) data. Details regarding application of high pressure SAXS/WAXS technique at CHESS B1/B2 beamline could be found here[S1] and the references therein. The pressure-dependent volume of the pore structure unit cell (V_P) was determined by fitting a Gaussian peak-shape to the background subtracted x-ray scattering peak occurring near 0.065 A^{-1} in Q-space (inset of Fig. 2a).[S2–S4] The fractional change in the pore-structure unit cell volume (V_P/V_0) is calculated by taking the ratio of V_P, which is the volume at pressure P, to $V_{0,}$ which is the volume at 0.1 MPa. Using a similar (Birch) equation of state functional formalism adopted by Xu et al.[S5] yields an estimate for the value of the first derivative of the bulk modulus with respect to pressure $\kappa' = 2.6(9)$ for mesoporous K_xWO_3, in good agreement with the value obtained for bulk WO_3.[S5]

Rietveld Refinement of the MAXS and WAXS Data

The "I *vs.* Q" data for the mesoporous sample and the NIST CeO_2 standard (SRM 674b) were obtained after integrating the 2D powder diffraction data using FIT2D software.[S6] The contribution to the peak shape due to the experimental setup was obtained after performing a Rietveld refinement of the CeO_2 standard. These parameters, which account for instrumental broadening of the peak shape, were kept fixed for refinement of the x-ray diffraction (i.e., the MAXS and WAXS) data from the mesoporous sample. The refinement of the x-ray diffraction (XRD) data indicate that the mesoporous $K_{0.07}WO_3$ specimen contains an orthorhombic tungsten bronze (OTB) superstructure with space group *P*222 (initial structure from ICSD 88766 but with more atoms and larger lattice constants), a Keggin-like $K_3PW_{12}O_{40}$ phase with space group $Pn\bar{3}m$ (initial structure from ICSD-165409) and an underlying monoclinic γ-WO_3 phase (initial structure from ICSD-80056) with space group $P12_1/n1$ yielding a value of R_{wp} = 6.99 and R_p = 4.63. The results of the structural refinement are summarized in Table S1. The OTB phase has lattice parameters a = 8.121(6) Å, b = 5.857(3) Å and c = 8.255(4) Å. The monoclinic unit cell of γ-WO_3 phase has lattice parameters a_m = 7.388(9) Å, b_m = 7.490(8) Å, c_m = 7.685(8) Å and β = 90.81(9)°. The cubic Keggin-like $K_3PW_{12}O_{40}$ phase has a lattice constant a_c = 11.587(2) Å. The prominent peaks corresponding to the K-bearing phases are indicated by the black vertical arrows in Fig. 3b. The monoclinic structural phase predominates in this material: the refinement yields a weight percentage composition of ~ 81.7% for the monoclinic γ-WO_3, ~ 8.1% for the OTB phase, and ~ 9.7% for the Keggin-like $K_3PW_{12}O_{40}$ phase. The remaining ~0.5% contribution is due to the reflections originating from the Rhenium gasket used in the diamond anvil cell, marked by '*' in Fig. 3b. The high intensity of the {002} triplets between Q ~ 1.6 − 1.8 $Å^{-1}$ is indicative of the presence of a predominantly monoclinic (γ-WO_3) phase which is confirmed by the refinement results. Although this could not be directly detected using TEM, it is plausible that the occurrence of the K-bearing Keggin-like $K_3PW_{12}O_{40}$ and OTB phases is highly correlated

but differentiated by the presence or lack-thereof of P, respectively, in the mesoporous material.

Rietveld refinement of the XRD data was also attempted with mixed phases of various other structures where K_xWO_3 phases with structures given by space group nos. 16, 25, 62, and 143 were attempted in combination with the γ-WO_3, $K_3PW_{12}O_{40}$ phase and the Re-impurity peaks. This additional analysis was made in order to cross check our refinement results and also to test for whether any other experimentally observed intergrowth and/or hexagonal tungsten bronzes (ITB or HTB)[S7–S12] are present in the material. We also attempted a refinement where ε-WO_3 (triclinic phase) was tried in combination with γ-WO_3, $K_3PW_{12}O_{40}$ and Re peaks. Refinement with any of these other phases did not provide satisfactory results. In the case of the absence of an additional ε-WO_3 component in the material, this result is reasonable as this phase is typically observed at low temperatures (below – 43 °C).[S13] The final refined structure with γ-WO_3 + OTB K_xWO_3 + Keggin-like $K_3PW_{12}O_{40}$ phases gives the best fit and is consistent with Raman results and TEM observations.

Table S1. Results of Rietveld Refinement of XRD data: Values of the fraction atomic coordinates (x, y, z), site occupancy, Debye-Waller factor B and the lattice parameters after Rietveld refinement of the three structures.

Keggin (SG: $Pn\bar{3}m$); a = 11.587(2) Å; V = 1555.7(8) Å^3					
Atoms	x	y	z	Site occupancy	B (Å^2)
W 1	0.527(9)	0.527(9)	0.738(2)	1.0	0.99
P 1	0.25	0.25	0.25	1.0	1.0
O 1	0.658(7)	0.658(5)	0.658(8)	1.0	1.03
O 2	0.875(5)	0.875(4)	0.002(5)	1.0	0.91
O 3	0.641(8)	0.641(5)	0.482(9)	1.0	0.95
O 4	0.437(9)	0.437(6)	0.741(9)	1.0	0.99
K 1	0.25	0.75	0.75	0.9	0.03
γ-WO_3 (SG: $P12_1/n1$); a = 7.388(9) Å; b = 7.490(8) Å; c = 7.685(8) Å; β = 90.81°(9); V = 425.3(2) Å^3					
W 1	0.239(9)	0.049(8)	0.296(9)	1.0	0.92
W 2	0.255(7)	−0.006(9)	0.769(7)	1.0	0.91
O 1	0.001(1)	0.037(7)	0.212(5)	1.0	0.95
O 2	−0.003(2)	0.463(5)	0.216(8)	1.0	0.97
O 3	0.282(5)	0.260(3)	0.287(9)	1.0	0.99

O 4	0.211(7)	0.260(5)	0.731(6)	1.0	0.96
O 5	0.286(3)	0.039(7)	0.006(3)	1.0	0.99
O 6	0.285(4)	0.485(8)	−0.008(3)	1.0	1.01
OTB (SG:*P*222); a = 8.121(6) Å; b = 5.857(3) Å; c = 8.255(4) Å; V = 392.6(4) Å^3					
K 1	0.5	0.285(6)	0.5	1.0	1.0
W 1	0.5	0	0	1.0	1.0
W 2	0.5	0.5	0	1.0	1.0
W 3	0.872(5)	−0.014(9)	0.223(9)	1.0	0.98
W 4	0.800(5)	0.437(9)	0.217(9)	1.0	0.95
O 1	0.85	0	0	1.0	0.92
O 2	0.85	0.5	0	1.0	0.91
O 3	0	0	0.3	1.0	0.99
O 4	0	0.5	0.3	1.0	0.97
O 5	0.64	0	0.18	1.0	0.96
O 6	0.64	0.5	0.18	1.0	0.95
O 7	0.79	0	0.5	1.0	0.94
O 8	0.79	0.5	0.5	1.0	0.97
O 9	0.5	0.25	0	1.0	0.93
O 10	0.8	0.25	0.25	1.0	0.99
O 11	0.8	0.75	0.25	1.0	0.91

Raman Measurements and Analysis

Measurements of the vibrational phonon modes were made using a Horiba LabRAM HR800 micro Raman setup and a 50mW 532 nm narrow bandwidth solid-state laser source. Filters were put in place to lower the intensity of the incident light on the sample and Stokes Raman excitation lines were measured in the experiments. Our fitting of the Raman spectrum measured from the as prepared mesoporous $K_{0.07}WO_3$ is shown in Fig. S1 and the results are summarized in Table S2. Multiple pseudo-Voigt peak shapes were used in order to determine the peak positions and peak widths in the Raman spectrum.[S14]

Table S2. Peak positions, widths and types after peak-fitting of Raman spectrum: Fitting of the Raman results. Values of the fitting parameters using pseudo-Voigt peak shapes for the plot of Fig. S1 are tabulated. Here, w is the peak width, x_c is the peak center and the value of m determines the pseudo Voigt line-shapes: m = 0 means pure Gaussian and m = 1 implies pure Lorentzian line-shape.

Peak no.	x_c (cm^{-1})	w (cm^{-1})	m
1	65.1 ± 0.2	10.1 ± 0.4	0
2	85.8 ± 0.9	17.9 ± 2.5	0
3	132.1 ± 0.3	16.8 ± 0.8	1
4	197.6 ± 1.1	37.8 ± 2.9	0
5	264.6 ± 0.6	38.9 ± 1.5	1
6	294.8 ± 3.0	33 ± 12.3	1
7	323.0 ± 3.4	32.4 ± 9.3	0
8	367.0 ± 3.8	31.5 ± 10.0	0
9	427.0 ± 2.6	40.5 ± 7.1	0
10	648.0 ± 1.0	96.3 ± 2.0	1
11	700.6 ± 0.3	49.1 ± 1.1	1
12	802.7 ± 0.1	29.8 ± 0.1	1
13	989.0 ± 1.9	5.3 ± 3.2	1
14	1004.0 ± 1.2	7.3 ± 2.8	1
15	1141.0 ± 2.2	105.0 ± 9.0	1

Table S3 shows the Raman band values from measurements made on the periodic FDU-12 type mesoporous $K_{0.07}WO_3$ sample in comparison to the Raman shifts observed by da Silva *et al.*[S15] from measurements of a bulk $Cs_4W_{11}O_{35}$ hexagonal tungsten bronze, along with the vibrational mode assignments made from lattice dynamics theory.[S15] The incorporation of alkali ions (Li^+ and H^+) has been observed to cause distortion of the octahedral units and W^{6+} reduction to W^{5+} in bulk M_xWO_3, giving rise to W^{5+}–O and W^{5+}=O bending modes close to 330 cm^{-1} and 450 cm^{-1}.[S16] It seems reasonable that the incorporation of the K^+ ion would cause similar effects in mesoporous $K_{0.07}WO_3$.

Table S3. Comparison of Raman bands of K_xWO_3 with literature: A comparison of the predominant WO_3 Raman band values and those attributed to the OTB phase measured from our mesoporous $K_{0.07}WO_3$ to the Raman bands measured by da Silva *et al.* from a $Cs_4W_{11}O_{35}$ hexagonal tungsten bronze.[S15] The vibrational mode assignments made from lattice dynamics theory by Da Silva *et al*. [S15] are also included.

Our Study (cm^{-1})	Da Silva et al. (cm^{-1})	Vibrational mode (as assigned by da Silva et al.[S15])
803	799	Apical O vibration within WO_6 octahedra
701	718-719	Apical O vibration within WO_6 octahedra
648	651	O stretching mode in plane of hexagonal ring of WO_6 octahedra
427	414	O-W-O bending modes in plane of hexagonal ring of WO_6 octahedra
367	360	Hex ring O-W-O bending modes + librations of WO_6 octahedra

UV-Vis Measurements

A suspension of the mesoporous FDU-12-type $K_{0.07}WO_3$ was prepared in DI water and allowed to evaporate on an ordinary microscope glass slide to create a film of the material. The UV-Vis transmission/absorption spectra (with the glass slide used as a reference) of the mesoporous $K_{0.07}WO_3$ film were measured using an Ocean Optics HR 4000 spectrophotometer and the OceanView 1.4 acquisition software. A fiber-optic coupled DT-Mini-2 deuterium/tungsten-halogen lamp source (Ocean Optics) was used for light excitation of the sample. The OceanView 1.4 acquisition software enables collection of spectral readings on an instantaneous basis: The accumulated spectra were collected in ~3 ms. The transmission spectral measurements were repeated several times to ensure collection of reproducible data. The energy gap of mesoporous $K_{0.07}WO_3$ is estimated from the intersection of the fitted line of the $(\alpha \cdot h\nu)^{1/2}$ quantitity at the zero point with the energy ($h\nu$) axis as shown in Fig S2.

N_2 Sorption Measurements

The N_2 sorption measurements of the mesoporous $K_{0.07}WO_3$ material were made using a Quantachrome Autosorb-1 gas-sorption analyzer. The samples were degassed in vacuum at

150 °C overnight prior to the N_2 sorption measurements. The specific surface area of the sample was calculated using the Brunauer-Emmett-Teller (BET) method. The results of the N_2 sorption measurements along with the corresponding DFT pore-size distribution of the mesoporous K_xWO_3 material are shown in Fig. S3. DFT calculations gave an estimate of the total pore volume as 0.6 cm^3/g and a narrow pore-size distribution with the pore width to be approximately 12.5 nm. This is in reasonable agreement, within experimental errors, with the TEM measurements of Fig. 1a.

Ab Initio Calculations

The bulk modulus (κ) of various WO_3 and K-bearing WO_3 phases were calculated using *ab-initio* molecular dynamics (AIMD) simulations within the Density Functional Theory (DFT) approximation as implemented in VASP.[S17,S18] The approach implemented in VASP is based on a finite-temperature local-density approximation and an exact evaluation of the instantaneous electronic ground state at each MD-step.[S17,S18] The AIMD simulations were performed with a 2 fs time step. We employed gamma point sampling and the projected augmented wave (PAW)[S19] potentials with the GGA-PBE[S20] exchange and correlation approximations. A constant energy cut-off of 500 eV was used and the electronic convergence was set to 10^{-4} eV to ensure a high precision on the average volume/pressure values. The bulk modulus values were calculated from the relaxed unit cell volume dependence on pressure using NVT/NPT simulations. Using a similar methodology as in the case of the pressure-dependent small angle x-ray scattering (SAXS) experiments, the bulk modulus was estimated by taking the inverse slope of a linear relationship of the fractional change in the unit cell volume (V_P/V_0) with pressure, where V_P and V_0 are the volumes at high and ambient pressure, respectively. For molecular dynamics simulations of a periodic mesoporous WO_3, a WO_3 monoclinic unit cell was assembled and then relaxed by density functional theory (DFT) calculations at three different pressures (0.1, 2.8 and 4.6 GPa). This was necessary in order to

properly account for torsional buckling of the WO_6 polyhedra in monoclinic WO_3 under pressure. The monoclinic unit cells, relaxed at each pressure, were repeated to form cubes (28 nm on each side) of about 1.5 million atoms. Pores were carved out in a face-centered cubic arrangement, with a variety of pore sizes to control porosity. LAMMPS software[S21] was used in conjunction with Buckingham potentials for W and O[S22] to make the molecular dynamics (MD) simulations. Hydrostatic pressure was applied to the porous blocks until an equilibrium volume was reached. The bulk moduli were determined from the linear trend of V_P/V_0 with pressure, where V is the volume of the simulation cell. By repeating this procedure for simulation boxes having varying pore volumes, the effect of porosity on the bulk modulus was determined using MD simulations. Additional details on methods and procedures are given in the Supplementary Information.

The AIMD results for the calculation of the bulk modulus of monoclinic, orthorhombic, and hexagonal WO_3 as well as hexagonal $K_{0.33}WO_3$, are shown in Table S4. The bulk modulus was calculated for the Keggin $K_3PW_{12}O_{40}$ cubic structure as follows: First, the elastic coefficients (c_{ij}) were calculated at the ground state by use of strain-stress analysis[S23] and AIMD simulations. The structure was initially fully relaxed and subsequently a small strain was applied to each independent ε_j strain element. The six stress component σ_{ij} were calculated from the strain following the set of linear elastic equations:

$$\sigma_{ij} = \sum_{ij} c_{ij} \varepsilon_j$$

For a cubic crystal structure, the bulk modulus (κ) can be calculated from the elastic constants using $\kappa = (2\ C_{12} + C_{11})/3$. We applied a full occupancy with respect to all of the atomic positions for the Keggin structure: The calculated bulk modulus value (κ = 37.5 GPa) should be treated as an upper estimate.

Table S4. AIMD results: Bulk modulus values calculated using AIMD for various WO_3 and K-bearing WO_3 phases.

System	Space Group	Bulk modulus (GPa)
Monoclinic WO_3	P121/n1	50.7
Orthorhombic WO_3	P222	132.8
Hexagonal WO_3	P6/mmm	171.7
Hexagonal $K_{0.33}WO_3$	P6/mmm	194.1

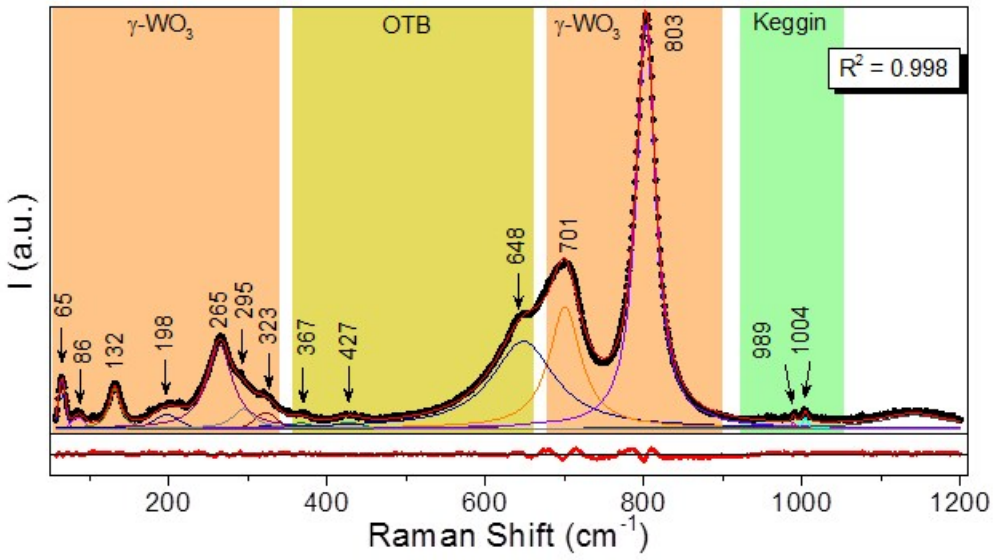

Fig. S1. Peak-fitting of Raman Spectrum: Peak fitting of the Raman spectrum measured from the as prepared mesoporous $K_{0.07}WO_3$. The spectrum was fit with combinations of multiple pseudo Voigt peak shapes. The coefficient of determination ($R^2 = 0.998$) of the fit is noted in the Figure and the peak positions (rounded to zero decimal point) are also shown. Table S3 gives the details of the fitting parameters.

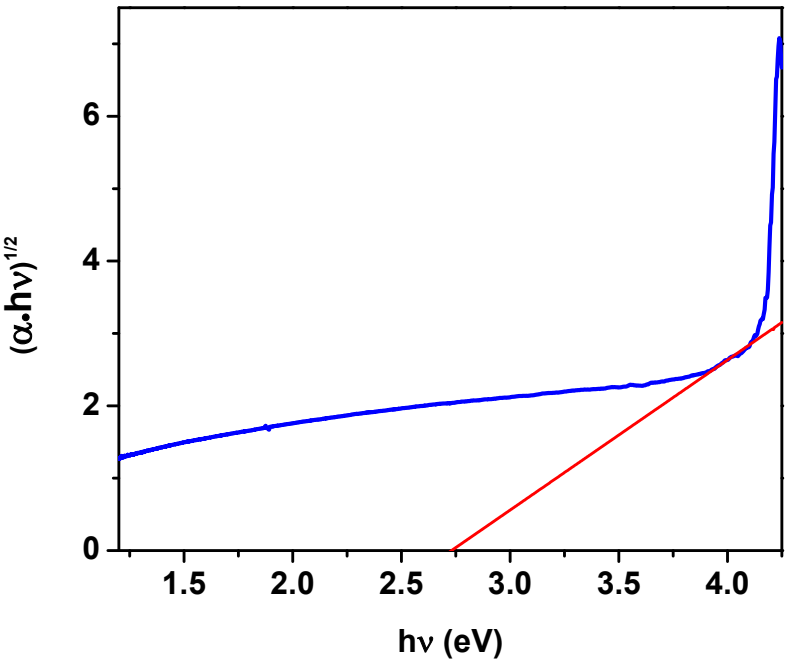

Fig. S2 The $(\alpha \cdot h\nu)^{1/2}$ quantitity vs photon energy ($h\nu$) as determined from the UV-Vis absorption data measured (at room temperature) from mesoporous $K_{0.07}WO_3$. The extrapolated fitted line intersects the energy axis at ~2.7 eV.

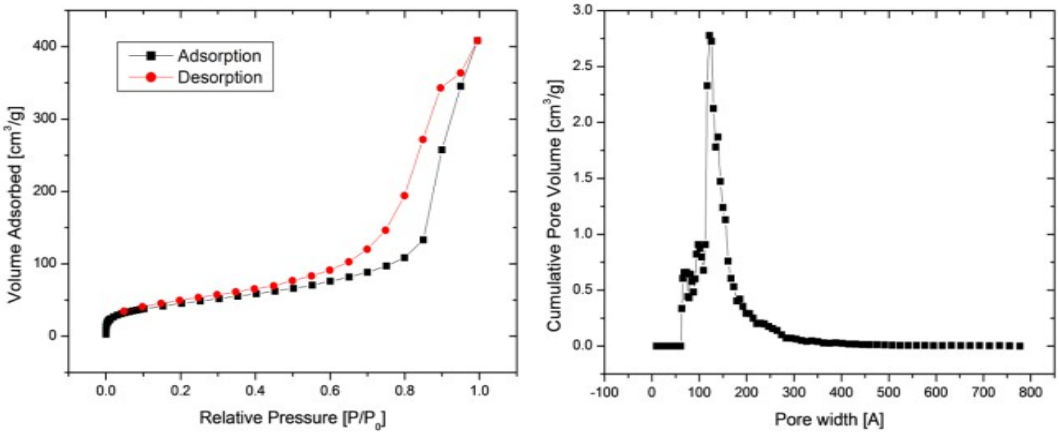

Fig. S3 (a) N_2 adsorption-desorption isotherms and (b) pore volume as a function of pore width of mesoporous $K_{0.07}WO_3$. The data were collected on a sample etched in 10% HF for ~6 hours.

References

S1. T. Wang, R. Li, Z. Quan, W. S. Loc, W. A. Bassett, H. Xu, Y. C. Cao, J. Fang and Z. Wang, *Adv. Mater.*, 2015, **27**, 4544–4549.

S2. R. A. Mayanovic, H. Yan, A. D. Brandt, Z. Wang, M. Mandal, K. Landskron and W. A. Bassett, *Microporous Mesoporous Mater.*, 2014, **195**, 161–166.

S3. A. M. Lapeña, J. Wu, A. F. Gross and S. H. Tolbert, *J. Phys. Chem. B*, 2002, **106**, 11720–11724.

S4. J. Wu, X. Liu and S. H. Tolbert, *J. Phys. Chem. B*, 2000, **104**, 11837–11841.

S5. Y. Xu, S. Carlson and R. Norrestam, *J. Solid State Chem.*, 1997, **132**, 123–130.

S6. A. P. Hammersley, *Eur. Synchrotron Radiat. Facil. Intern. Rep. ESRF97HA02T*, 1997.

S7. P. G. Dickens and M. S. Whittingham, *Q Rev Chem Soc*, 1968, **22**, 30–44.

S8. A. Hussain and L. Kihlborg, *Acta Crystallogr. A*, 1976, **32**, 551–557.

S9. T. Wolfram and S. Ellialtioglu, *Electronic and optical properties of d-band perovskites*, Cambridge University Press Cambridge, 2006.

S10. M. Johnsson and P. Lemmens, *Crystallography and chemistry of perovskites*, John Wiley & Sons Ltd, Chichester, UK, 2007, vol. 4.

S11. A. Hussain, *Acta Chem Scand A*, 1978, **32**.

S12. R. Sharma and L. Kihlborg, *Mater. Res. Bull.*, 1981, **16**, 377–380.

S13. E. Salje, *Ferroelectrics*, 1976, **12**, 215–217.

S14. G. K. Wertheim, M. A. Butler, K. W. West and D. N. E. Buchanan, *Rev. Sci. Instrum.*, 1974, **45**, 1369–1371.

S15. K. P. da Silva, W. Paraguassu, M. Maczka, S. AG Filho, P. T. C. Freire and J. Hanuza, *J. Raman Spectrosc.*, 2011, **42**, 474–481.

S16. S.-H. Lee, H. M. Cheong, C. E. Tracy, A. Mascarenhas, D. K. Benson and S. K. Deb, *Electrochimica Acta*, 1999, **44**, 3111–3115.

S17. G. Kresse and J. Furthmüller, *Comput. Mater. Sci.*, 1996, **6**, 15–50.

S18. G. Kresse and J. Furthmüller, *Phys. Rev. B*, 1996, **54**, 11169.

S19. P. E. Blöchl, *Phys. Rev. B*, 1994, **50**, 17953.

S20. J. P. Perdew, K. Burke and M. Ernzerhof, *Phys. Rev. Lett.*, 1996, **77**, 3865.

S21. S. Plimpton, *J. Comput. Phys.*, 1995, **117**, 1–19.

S22. M. S. Islam, S. Lazure, R. Vannier, G. Nowogrocki and G. Mairesse, *J. Mater. Chem.*, 1998, **8**, 655–660.

S23. O. H. Nielsen and R. M. Martin, *Phys. Rev. Lett.*, 1983, **50**, 697.